



# Promotional effect of Ga for Ni<sub>2</sub>P catalyst on hydrodesulfurization of 4,6-DMDBT

Jung-Geun Jang, Yong-Kul Lee\*

Laboratory of Advanced Catalysis for Energy and Environment, Department of Chemical Engineering, Dankook University, 152 Jukjeonro, Yongin 16890, South Korea

## ARTICLE INFO

### Keywords:

Ni<sub>2</sub>P  
Ga  
4,6-DMDBT  
Direct desulfurization  
HDS

## ABSTRACT

Ni<sub>2</sub>P catalysts supported on SiO<sub>2</sub> and Ga-SiO<sub>2</sub> were prepared by incipient wetness impregnation technique, and the effect of the electronic properties of Ni<sub>2</sub>P on hydrodesulfurization (HDS) performance was studied. X-ray diffraction (XRD), X-ray absorption near edge structure (XANES), and in situ FT-IR with CO adsorption studies were used to examine structural and electronic properties of the supported Ni<sub>2</sub>P catalysts. The catalytic activity in hydrodesulfurization (HDS) was measured at 3.0 MPa and at three different temperatures of 613, 628, and 643 K in a three-phase fixed bed reactor using a model feed containing 500 ppm S as 4,6-DMDBT, 6000 ppm S as DMDS, 100 ppm N as quinoline, 1 wt% tetralin, and 0.5 wt% n-nonane in n-tridecane balance. In both cases, the HDS conversion was very high over 90%. For the product distributions, the Ni<sub>2</sub>P/SiO<sub>2</sub> maintained a low direct desulfurization (DDS) selectivity at 26.5%, while the Ni<sub>2</sub>P/Ga-SiO<sub>2</sub> exhibited higher DDS selectivity of 32.1% at 643 K. The Ni K-edge XANES and CO-adsorbed FT-IR analysis confirmed the electron enriched property of Ni<sub>2</sub>P on SiO<sub>2</sub>, but with the electron deficiency of Ni<sub>2</sub>P phase supported on Ga-SiO<sub>2</sub> support. These results thus suggest that the electron deficient Ni<sub>2</sub>P favors  $\sigma$ -bonding with S compounds to promote direct desulfurization of 4,6-DMDBT.

## 1. Introduction

Over the past few decades, global environmental regulations have become more stringent, and restrictions on sulfur content in fuels such as diesel and gasoline have also been strengthened [1–9]. Furthermore, the International Maritime Organization (IMO) has significantly restricted a global sulfur limit in marine fuel, which was an existing 3.5%, to 0.5% from 2020 [10].

Oil refiners have generally used hydrodesulfurization (HDS) processes with metal sulfide catalysts to produce ultra-low sulfur fuels [4,11]. In order to meet the environmental regulations fuels it is inevitable to remove refractory sulfur compounds like 4,6-dimethyldibenzothiophene (4,6-DMDBT), which is difficult to desulfurize. As crude oils get heavier, the amount of refractory sulfur compounds in the feedstock will increase [1], making it difficult to satisfy the environmental regulations by using the conventional CoMo and NiMo sulfide catalysts [12]. The transition metal phosphide catalyst has been introduced as a new class of highly active hydrotreating catalysts and has attracted attention as a potential substitute for conventional catalysts [13–17]. Especially, Ni<sub>2</sub>P is known to have the highest activity among the metal phosphide catalysts, even presenting two-fold intrinsic activity relative to CoMo sulfide catalyst in the HDS of dibenzothiophene

(DBT) [13].

The HDS of 4,6-DMDBT is known to occur via two reaction pathways, hydrogenation (HYD) and direct desulfurization (DDS), depending on the type of bond between 4,6-DMDBT and the catalytic active site [3,18,19]. The HYD pathway is known to occur via the formation of  $\pi$ -bond between aromatic rings of 4,6-DMDBT and the catalytic active site, in which  $\pi$ -electrons of aromatic rings of 4,6-DMDBT adsorb on the catalyst [3]. In this case, hydrogenation of aromatic rings takes priority over C–S bond cleavage step [3]. On the other hand, the DDS pathway is induced by forming the  $\sigma$ -bond between the lone electron pair of S atom of the thiophenic S compounds and catalytic active site, and proceeds the C–S bond cleavage without saturating the aromatic rings [19]. However, in the case of forming the  $\sigma$ -bond between 4,6-DMDBT and the catalyst, it is disturbed by the steric hindrance formed by alkyl group around the S atom particularly over the conventional sulfide catalysts [3,20]. Therefore, when the 4,6-DMDBT is adsorbed on the catalyst,  $\pi$ -bond is mainly formed rather than  $\sigma$ -bond, and thus desulfurization is mainly achieved through the HYD pathway rather than the DDS pathway [3,21]. The Ni<sub>2</sub>P catalyst favors the HYD pathway rather than the DDS route in the HDS of 4,6-DMDBT, while the active site of the phosphides is different from the sulfides, the former being a spherical surface and the latter being a

\* Corresponding author.

E-mail address: [yolee@dankook.ac.kr](mailto:yolee@dankook.ac.kr) (Y.-K. Lee).

<https://doi.org/10.1016/j.apcatb.2019.01.087>

Received 8 August 2018; Received in revised form 15 January 2019; Accepted 18 January 2019

Available online 31 January 2019

0926-3373/© 2019 Elsevier B.V. All rights reserved.

hexagonal rim-site [22,23]. The product selectivity of the HDS has a crucial impact on product quality as well as  $H_2$  consumption, where the DDS pathway consumes less amount of  $H_2$  than the HYD pathway, being cost effective. Accordingly, catalytic studies have been made to improve the DDS path selectivity by adding other metals to  $Ni_2P$  catalyst [24–26]. Oyama et al. studied the bimetallic phosphide catalysts of Ni and Fe (NiFeP), greatly improving the DDS selectivity of 4,6-DMDBT from 12% to 85%, while maintaining high HDS activity of  $Ni_2P$  [25,27]. Li et al. demonstrated the promotional effect of Ce on  $Ni_2P$ /SBA-15 catalysts, apparently enhancing the DDS selectivity of dibenzothiophene (DBT), in which the higher interaction of CeOx with  $Ni_2P$  gave rise to an increase in the DDS selectivity [26]. These findings indicate the possibility of changing product selectivities of the HDS using promoters affecting the electronic properties on active centers of  $Ni_2P$ .

As for the various promoters Ga was found to promote the DDS selectivity in the HDS of 4,6-DMDBT over the conventional HDS catalysts such as CoMo [28], NiMo [29,30], and W [31,32] sulfides. Vrinat group reported a series of papers on the promoting effect of Ga on sulfide catalysts [28,30–32], in which Ga interacts with tetrahedral sites of alumina supports, allowing the formation of active Ni(Co)MoS<sub>2</sub> phases. In this study the DDS selectivity of the HDS of 4,6-DMDBT was found to be 35 and 16% higher over the 0.6 and 1.2 wt% Ga added NiMo catalysts than that of a NiMo catalyst [30], but the proper correlation between the product selectivity and the Ga addition was not verified. Given the similar catalytic nature of  $Ni_2P$  with NiMoS catalysts, the addition of Ga may change the product selectivity of the HDS. It is thus a major goal of this study to investigate the effect of Ga addition on the physical properties of  $Ni_2P$  catalysts and on the catalytic activity in the HDS of 4,6-DMDBT. More emphasis was made on the XANES analysis for the catalysts to verify electronic properties of the catalysts.

Overall, it was demonstrated that the Ga promoted  $Ni_2P$  catalyst shows than lower surface electron density than the conventional  $Ni_2P$ , promoting the DDS pathway in HDS of 4,6-DMDBT via the formation of the  $\sigma$ -bond with the thiophenic S.

## 2. Experimental

### 2.1. Synthesis of supported $Ni_2P$ catalysts

For Ga-SiO<sub>2</sub> an aqueous solutions of gallium nitrate ( $Ga(NO_3)_3$ , Alfa, 99.9%) as a Ga precursor was added to commercially available silica (Cab-O-Sil, L90, 90 m<sup>2</sup>/g) using incipient wetness impregnation. The amount of Ga added to the silica was 1.0% by weight. After impregnation, the mixture was dried at 353 K for 12 h, calcined at 723 K for 4 h, cooled to room temperature, and then ground into powder.

The  $Ni_2P$ /SiO<sub>2</sub> catalyst was prepared by incipient wetness impregnation using dissolved nickel nitrate hexahydrate ( $Ni(NO_3)_2 \cdot 6H_2O$ , Alfa, 98%) and ammonium phosphate ( $(NH_4)_2HPO_4$ , Samchun, 99%) in distilled water. The amount of Ni loading was fixed at 1.0 mmol Ni per 1 g of the support having an initial P / Ni molar ratio of 2.0. After impregnation, the catalyst sample was dried at 353 K for 12 h, calcined at 723 K for 4 h, then cooled to room temperature. The oxidic sample was reduced in a quartz U-tube reactor by temperature-programmed reduction (TPR) from room temperature to 873 K at 5 K min<sup>-1</sup> and held at 873 K for 2 h in a  $H_2$  flow (100 cm<sup>3</sup> min<sup>-1</sup> g<sup>-1</sup> loaded sample). After TPR, the catalyst sample was cooled to room temperature and passivated at 100 cm<sup>3</sup> min<sup>-1</sup> of 0.2 mol% O<sub>2</sub>/He flow for 4 h. The  $Ni_2P$ /Ga-SiO<sub>2</sub> was prepared in the same manner using the prepared Ga-SiO<sub>2</sub> as a support.

### 2.2. Characterization of catalyst samples

$H_2$ -TPR profiles were measured to identify the reduction characteristics of the oxidic precursors. 0.20 g of the samples were loaded in

a quartz U-tube reactor, and were reduced in 100 cm<sup>3</sup> min<sup>-1</sup> of  $H_2$  flow at a heating rate of 2.5 K min<sup>-1</sup> from 298 to 1123 K, and held at 1123 K for 0.5 h, which was monitored by a mass spectrometer (HP 5973 inert).

CO chemisorption uptake measurements were used to examine the dispersion of  $Ni_2P$  particles on the supports. Before the measurements, the passivated catalyst samples were re-reduced under 100 cm<sup>3</sup> min<sup>-1</sup> of  $H_2$  flow at 723 K for 2 h and cooled to room temperature in He atmosphere. After then, pulses (100  $\mu$ l) of CO in 100 cm<sup>3</sup> min<sup>-1</sup> of He carrier at room temperature were passed over the sample to measure the total dynamic gas uptake.

A Micromeritics ASAP 2010 micropore size analyzer was used to measure the specific surface area of the sample from the linear portion of BET plots ( $P/P_0 = 0.01$ – $0.10$ ) at 77 K. Approximately 0.15 g of catalyst was placed in a quartz tube. Before the measurement, the sample was degassed at 403 K for 2 h, and then cooled to room temperature. The surface area was determined according to the BET method.

The X-Ray diffraction (XRD) patterns of the samples were measured using a diffractometer (Rigaku DMAX-2500) operated at 60 kV and 300 mA with Cu K $\alpha$  radiation ( $\lambda = 0.15418$  nm). Crystallite sizes were calculated using the Scherrer equation,  $D_c = K\lambda / \beta \cos(\theta)$ , where  $\lambda$  is the wavelength of the X-ray radiation,  $\beta$  is the peak width in radians at half-maximum,  $K$  is a constant taken as 0.9 corrected for instrumental broadening, and  $2\theta$  is the Bragg angle of diffraction.

The chemical composition of the samples was determined by inductively coupled plasma-atomic emission spectroscopy (ICP-AES) (PerkinElmer, Model Optima 8300).

Transmission electron microscope (TEM) images and energy dispersive X-ray (EDX) spectrums were obtained using a JEOL JEM-2010 electron microscope operating at 200 kV. Samples were prepared by soaking a carbon-coated copper grid into the solution containing catalysts dispersed in hexane.

The X-Ray absorption spectra at the Ni K-edge (8.333 keV) and the Ga K-edge (10.367 keV) of the reference and catalyst samples were measured in the energy ranges of 8.233–8.823 keV and 10.267–10.867 keV, respectively, using a synchrotron radiation at the beamline 8C of the Pohang Light Source (PLS). The X-ray ring at the PLS has a flux of  $5 \times 10^{12}$  photons s<sup>-1</sup> at 100 mA and 3 GeV. The X-ray single crystal at the beamline 8C is equipped with a Si (1 1 1) channel-cut monochromator and has an energy range capability of 4–22 keV. The samples were prepared in a kapton sealed glass cell to avoid air-exposure. Given that the light source equipped with Si (1 1 1) allows the energy scan step size of 0.5 eV in the absorption energy ranges for Ni and Ga, the comparison of the XANES spectra for the catalyst samples was based upon the white line intensity and the post edge shape.

Infrared spectra of CO chemisorption (CO-FTIR) were obtained for the passivated catalyst samples on Perkin Elmer Frontier FTIR spectrometer at 0.25 s data scan interval with a resolution of 1 cm<sup>-1</sup>. The samples were pressed into discs (~50 mg) and placed in a quartz IR cell with water-cooled KBr windows. Before the analysis, catalyst samples were pretreated in 100 cm<sup>3</sup> min<sup>-1</sup>  $H_2$  flow at 723 K for 2 h, then cooled to room temperature in a  $N_2$  flow, and exposed to CO flow until saturation was achieved.

### 2.3. Activity test

The catalytic HDS activity was measured at 3.0 MPa and three different temperatures of 613, 628, and 643 K and in an upflow, fixed-bed reactor using a model feed mixture containing sulfur, nitrogen, aromatic, and aliphatic compounds. The feed liquid was prepared by combining 500 ppm (0.05 wt%) sulfur as 4,6-DMDBT (Acros, 95%), 6000 ppm (0.6 wt%) sulfur as dimethyldisulfide (DMDS, Aldrich, 99%), 100 ppm (0.01 wt%) nitrogen as quinoline (Acros, 96%), 1.0 wt% aromatics as 1,2,3,4-tetrahydronaphthalene (tetralin, Aldrich, 99%), 0.5 wt% n-nonane (Alfa, 99%) as an internal calibration standard for GC analysis, and balance aliphatics of n-tridecane (TCI, 99.0%). Quantities of catalysts loaded in the reactor were 1.0 cm<sup>3</sup> for the catalysts with

corresponding liquid hourly space velocity (LHSV) of  $2.0 \text{ h}^{-1}$ . Before the reaction tests, the passivated catalysts were pretreated for 2 h at 723 K with  $100 \text{ cm}^3 (\text{NTP}) \text{ min}^{-1}$  of  $\text{H}_2$  flow. The liquid was delivered at  $0.03 \text{ cm}^3 \text{ min}^{-1}$  using a liquid pump and  $\text{H}_2$  was delivered at  $50 \text{ cm}^3 (\text{NTP}) \text{ min}^{-1}$ . The liquid products were collected at 1–2 h intervals and were analyzed with a Hewlett Packard 6890 N gas chromatograph, equipped with a  $0.25 \text{ mm i.d.} \times 30 \text{ m}$  dimethylsiloxane column (Hewlett Packard, DB-1) and a flame ionization detector. Reaction products were identified by matching retention times with commercially available standards as well as by GC–MS analysis. The GC–MS consisted of Hewlett Packard 6890 N gas chromatograph, equipped with a  $0.25 \text{ mm i.d.} \times 30 \text{ m}$  dimethylsiloxane column (Hewlett Packard, DB-1MS) and Agilent 5973 mass selective detector. The 4,6-dimethyldibenzothiophene (4,6-DMDBT) undergoes HDS via two parallel reaction pathways: (i) direct desulfurization (DDS) leading to the formation of 3,3-dimethylbiphenyl (3,3-DMBP) and (ii) prehydrogenation followed by desulfurization (HYD) giving first 4,6-tetrahydro- and hexahydrodibenzothiophenes, which are further desulfurized to methylcyclohexyltoluenes (MCHT) and dimethylbicyclohexyls (DMBCH). In this work, the HDS conversion and the selectivities are defined as:

$$\text{HDS conversion (\%)} = 100 \times \left( 1 - \frac{\text{MCHT} + \text{DMBCH} + 3,3\text{DMBP}}{4,6\text{DMDBT}_{\text{in}}} \right)$$

$$\text{HYD selectivity (\%)} = 100 \times \left( \frac{\text{MCHT} + \text{DMBCH}}{4,6\text{DMDBT}_{\text{in}} - 4,6\text{DMDBT}_{\text{out}}} \right)$$

$$\text{DDS selectivity (\%)} = 100 \times \left( \frac{3,3\text{DMBP}}{4,6\text{DMDBT}_{\text{in}} - 4,6\text{DMDBT}_{\text{out}}} \right)$$

### 3. Results and discussion

#### 3.1. Physical properties of $\text{Ni}_2\text{P}$ catalysts

Fig. 1 shows  $\text{H}_2$ -TPR profiles of the calcined oxidic precursors of  $\text{Ni}_2\text{P}/\text{SiO}_2$ ,  $\text{Ni}_2\text{P}/\text{Ga-SiO}_2$ , and  $\text{Ga-SiO}_2$  samples. The maximum reduction peak of  $\text{Ni}_2\text{P}/\text{SiO}_2$  was observed at around 850 K with a shoulder at 750 K, as also observed in the previous studies [15,33,34]. The asymmetric feature of TPR patterns for oxidic precursors of  $\text{Ni}_2\text{P}$  sample is related with an overlap of two different TPR patterns with a lower-temperature-reducible nickel oxide and a higher-temperature-reducible nickel phosphate, commonly found in lower-P and higher-P content samples, respectively [35]. In contrast, the reduction peak of  $\text{Ni}_2\text{P}/\text{Ga-SiO}_2$  sample was found to slightly shift to a higher temperature at 886 K without a shoulder that was observed in the reduction peak of  $\text{Ni}_2\text{P}/$

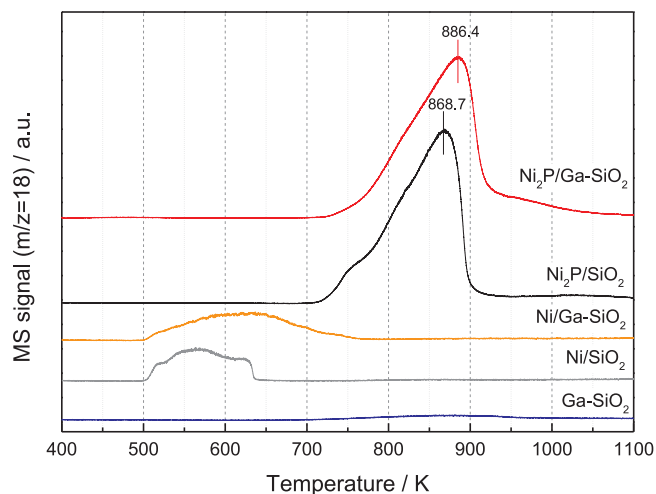


Fig. 1. TPR profiles of oxidic precursors of  $\text{Ni}_2\text{P}/\text{SiO}_2$ ,  $\text{Ni}_2\text{P}/\text{Ga-SiO}_2$ ,  $\text{Ni}/\text{SiO}_2$ ,  $\text{Ni}/\text{Ga-SiO}_2$ , and  $\text{Ga-SiO}_2$  samples.

$\text{SiO}_2$  sample, indicating that the addition of Ga delays the reduction of Ni-phosphate. On the other hand,  $\text{Ga-SiO}_2$  did not exhibit the reduction peak. Shao et al. also observed that  $\text{Ga}_2\text{O}_3\text{-SiO}_2$  was hardly reduced in  $\text{H}_2$ -TPR even in the high temperature region of 1000 K or more [36]. Considering that the surface areas of the two samples are similar to each other as listed in Table 1, the higher reduction temperature for the  $\text{Ni}_2\text{P}/\text{Ga-SiO}_2$  sample suggests that Ni-phosphate interacts with Ga species. The comparison of acidity of the  $\text{Ni}_2\text{P}/\text{SiO}_2$  and  $\text{Ni}_2\text{P}/\text{Ga-SiO}_2$  samples characterized by pyridine-adsorbed FTIR measurements (Fig. S1 of supplementary materials) shows very weak Lewis acidity in both cases, indicating that the addition of Ga does not alter the acidity of the  $\text{Ni}_2\text{P}/\text{SiO}_2$  catalyst.

Fig. 2 shows XRD patterns of the fresh and spent catalyst samples and  $\text{Ni}_2\text{P}$  reference. The  $\text{Ni}_2\text{P}/\text{SiO}_2$  exhibits a characteristic band of silica at  $10^\circ < 2\theta < 30^\circ$  and shows the  $\text{Ni}_2\text{P}$  characteristic peaks at  $40.5^\circ$ ,  $44.8^\circ$ , and  $47.5^\circ$ , similar to the  $\text{Ni}_2\text{P}$  reference (PDF-74-1385) and the previous studies [16,34,37]. Likewise,  $\text{Ni}_2\text{P}/\text{Ga-SiO}_2$  shows almost the same XRD patterns as  $\text{Ni}_2\text{P}/\text{SiO}_2$ . In both cases, the XRD patterns show the characteristic peaks of  $\text{Ni}_2\text{P}$  and silica, while the characteristic peaks for Ga or gallium oxide are not visible probably due to the small amount of Ga loading. Similarly, it was reported that the characteristic peaks of Ga metal or  $\text{GaOx}$  were not observed in the reduced  $\text{Ga-SiO}_2$  sample [36]. In addition, there is no noticeable difference in the XRD peaks between the fresh and spent samples, indicating that the crystallinity of the  $\text{Ni}_2\text{P}$  catalysts is maintained even after the reaction. Moreover, the crystallite size of  $\text{Ni}_2\text{P}$  calculated by the Scherrer's equation is about 10.2–11.7 nm (Table 1), and all samples show similar particle size to those observed in the previous studies [15,17]. These results suggest that addition of 1 wt% Ga slightly increases the reduction temperature, but does not affect the crystallinity of  $\text{Ni}_2\text{P}$ .

Fig. 3 displays TEM images of  $\text{Ga-SiO}_2$  and  $\text{Ni}_2\text{P}/\text{Ga-SiO}_2$ . The TEM image of  $\text{Ga-SiO}_2$  shows only the amorphous silica form and does not show the morphology of Ga. Likewise, the image for  $\text{Ni}_2\text{P}/\text{Ga-SiO}_2$  does not show the Ga phase, but only spherical  $\text{Ni}_2\text{P}$  particles well dispersed on  $\text{SiO}_2$ . Shao et al. also reported that Ga form is not visible in the TEM images if small amount of Ga less than 5 wt% is loaded on the  $\text{SiO}_2$  support [36]. On the other hand, the TEM-EDX analysis confirmed the presence of Ga in the  $\text{Ni}_2\text{P}/\text{Ga-SiO}_2$  catalyst, and its element map analysis shows a good spatial distribution of Ga together with Ni and P over the  $\text{SiO}_2$  support. Moreover, the presence of Ga in the  $\text{Ni}_2\text{P}/\text{Ga-SiO}_2$  samples was also confirmed by the ICP measurement as given in Table 1.

Fig. 4 shows the Ni K-edge X-ray absorption near edge structure (XANES) spectra for the fresh and spent catalyst samples and bulk  $\text{Ni}_2\text{P}$  for reference. The XANES region provides information about not only the local structure but also the oxidation state and relative electron density of the material [38]. It is shown that there is no noticeable difference in the  $\text{Ni}_2\text{P}$  phase of the XANES region. As with the XRD results in Fig. 2, all of the samples appear to form  $\text{Ni}_2\text{P}$  phase well. Therefore, a small amount of Ga does not have a significant effect on the phase of  $\text{Ni}_2\text{P}$  catalysts. However, the  $E_0$  value of  $\text{Ni}_2\text{P}/\text{Ga-SiO}_2$  (8.3378 keV) is observed slightly higher than that of  $\text{Ni}_2\text{P}/\text{SiO}_2$  i.e. 8.3373 keV. Previous studies reported that the increase of  $E_0$  value is due to the higher oxidation state of metal cation or electron deficiency of metal species in the catalyst [39]. Since the bulk  $\text{Ni}_2\text{P}$  phase does not change with the Ga addition, the increase in the  $E_0$  value can be attributed to the decrease in the surface electron density of  $\text{Ni}_2\text{P}$  rather than the phase change of Ni species. Therefore, these results thus suggest that the presence of Ga species around  $\text{Ni}_2\text{P}$  could withdraw a part of electrons from  $\text{Ni}_2\text{P}$ , lowering the electron density of  $\text{Ni}_2\text{P}$ .

In order to clarify the electronic property of Ga species, the Ga K-edge XANES spectra were also measured. Fig. 5 displays the Ga K-edge XANES spectra of the samples including  $\text{Ni}_2\text{P}/\text{Ga-SiO}_2$ ,  $\text{P}/\text{Ga-SiO}_2$ , and  $\text{Ga-SiO}_2$ . The calcined  $\text{Ga-SiO}_2$  shows a typical pattern of  $\beta\text{-Ga}_2\text{O}_3$  featuring a broad white line at around 10.370 eV, which is due to the electronic transition  $1s \rightarrow 4p$  for the Ga atoms with the mixed



**Table 1**  
Physical properties of the catalyst samples.

Catalyst	Ni loading (mmol g <sup>-1</sup> )	Condition	BET surface area (m <sup>2</sup> g <sup>-1</sup> )			Pore Volume (cm <sup>3</sup> g <sup>-1</sup> )		Average crystallite size <sup>c</sup> (nm)	P/Ni/Ga <sup>f</sup> (mol ratio)	CO uptake (μmol g <sup>-1</sup> )
			S <sub>total</sub> <sup>a</sup>	S <sub>micro</sub> <sup>b</sup>	S <sub>meso</sub> <sup>c</sup>	V <sub>micro</sub> <sup>b</sup>	V <sub>meso</sub> <sup>d</sup>			
Ni <sub>2</sub> P/SiO <sub>2</sub>	1.0	Fresh	77	12	65	0.005	0.484	10.8	0.89 / 1.00 / -	30.0
		Spent	73	11	62	0.004	0.532	11.7	0.68 / 1.00 / -	27.9
Ni <sub>2</sub> P/Ga-SiO <sub>2</sub>	1.0	Fresh	78	12	66	0.005	0.420	10.6	0.81 / 1.00 / 0.08	29.1
		Spent	75	8	67	0.003	0.484	10.2	0.67 / 1.00 / 0.08	27.9

<sup>a</sup> Obtained by BET measurement.

<sup>b</sup> Calculated by the t-plot method.

<sup>c</sup> S<sub>total</sub> - S<sub>micro</sub>.

<sup>d</sup> V<sub>total</sub> - V<sub>micro</sub>.

<sup>e</sup> Calculated by Scherrer equation,  $D_c = K\lambda / \beta \cos(\theta)$ .

<sup>f</sup> Measured by elemental analysis using ICP-AES.

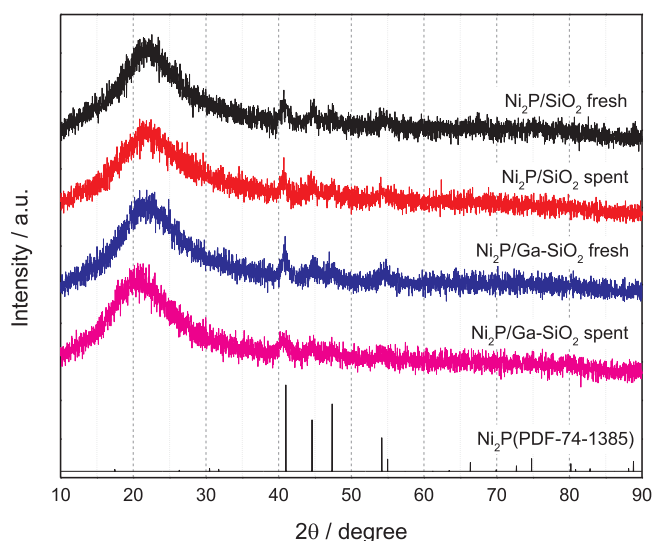
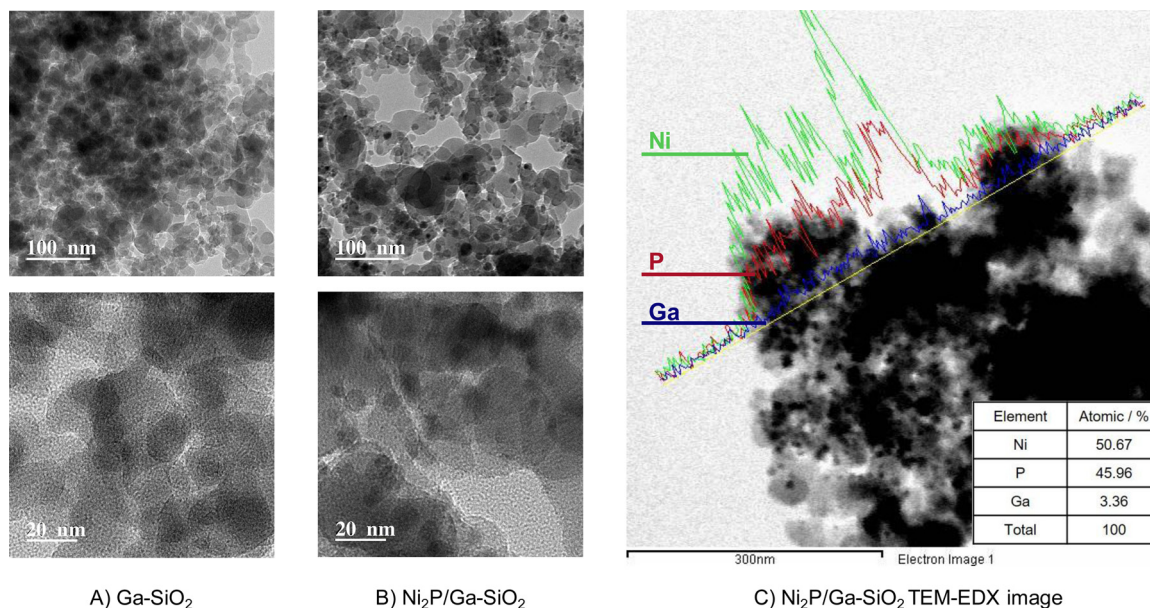


**Fig. 2.** XRD patterns for Ni<sub>2</sub>P/SiO<sub>2</sub> and Ni<sub>2</sub>P/Ga-SiO<sub>2</sub> samples.

coordination of tetrahedral GaO<sub>4</sub> and octahedral GaO<sub>6</sub> of β-Ga<sub>2</sub>O<sub>3</sub> [36,40]. The reduced Ga-SiO<sub>2</sub> sample, which was reduced at 873 K, shows a similar XANES spectrum with the calcined Ga-SiO<sub>2</sub> sample, indicating that β-Ga<sub>2</sub>O<sub>3</sub> is rarely reduced at the condition. This is consistent with the H<sub>2</sub>-TPR result in Fig. 1, in which the reduction behavior of Ga-SiO<sub>2</sub> was not identified. The introduction of P to the Ga-SiO<sub>2</sub> gave rise to a difference of the XANES spectrum featuring a sharp white line at 10.373 eV, labeled a, and the presence of post-edge structures, labeled b and c, which are assigned to characteristic peaks for GaPO<sub>4</sub> [41,42]. It is reported that GaPO<sub>4</sub> adopts tetrahedral GaO<sub>4</sub> structure, featuring a sharp white line. These results suggest that Ga has a strong interaction with phosphate even after reduction at a relatively high temperature over 873 K. In contrast to P-added Ga-SiO<sub>2</sub>, the introduction of Ni<sub>2</sub>P to the Ga-SiO<sub>2</sub> does not show the formation of GaPO<sub>4</sub> phase, while the XANES spectrum resembles β-Ga<sub>2</sub>O<sub>3</sub> phase but with a sharp white line intensity. Tourtin et al. showed that the addition of proper amount of phosphate to gallium oxide, Ga/P > 1.0, increases the white line intensity in Ga K-edge XANES of β-Ga<sub>2</sub>O<sub>3</sub> [41], suggesting that the interaction between Ga and P transforms the coordination of GaO<sub>4</sub> to GaO<sub>6</sub> structure [41]. Therefore, these results imply that the Ga species in Ni<sub>2</sub>P/Ga-SiO<sub>2</sub> exist mainly in the form of gallium oxide, while the interaction of excess P and GaOx increases the white line intensity of Ni<sub>2</sub>P/Ga-SiO<sub>2</sub> as much as that of octahedral GaO<sub>6</sub>.



A) Ga-SiO<sub>2</sub>

B) Ni<sub>2</sub>P/Ga-SiO<sub>2</sub>

C) Ni<sub>2</sub>P/Ga-SiO<sub>2</sub> TEM-EDX image

**Fig. 3.** TEM images for the catalyst samples: (A) Ga-SiO<sub>2</sub>, (B) Ni<sub>2</sub>P/Ga-SiO<sub>2</sub>, (C) TEM-EDX image for Ni<sub>2</sub>P/Ga-SiO<sub>2</sub>.

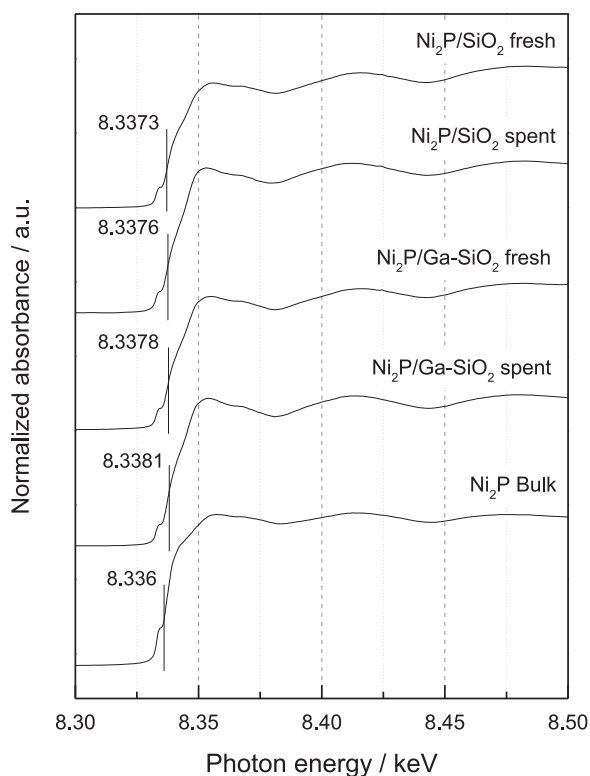


Fig. 4. Ni K-edge XANES spectra for  $\text{Ni}_2\text{P}/\text{SiO}_2$ ,  $\text{Ni}_2\text{P}/\text{Ga-SiO}_2$  samples and  $\text{Ni}_2\text{P}$  bulk.

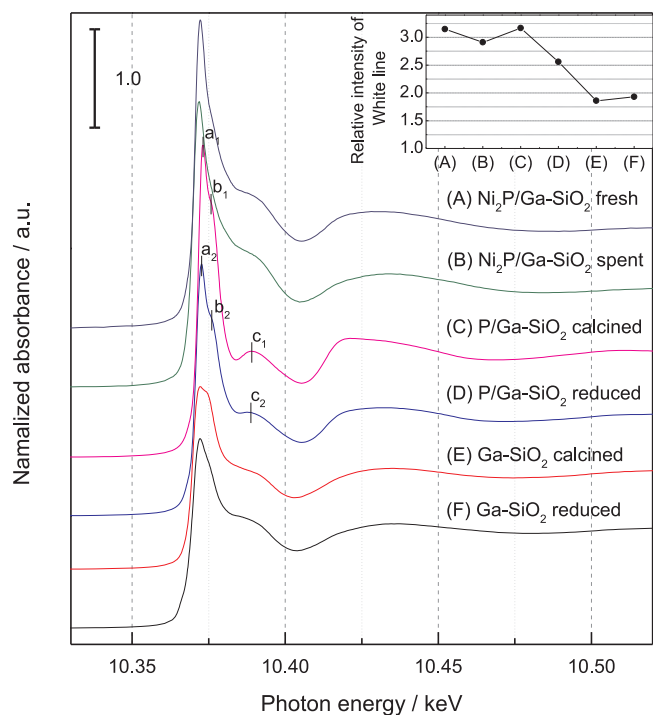


Fig. 5. Ga-K edge XANES spectra of (A)  $\text{Ni}_2\text{P}/\text{Ga-SiO}_2$  fresh, (B)  $\text{Ni}_2\text{P}/\text{Ga-SiO}_2$  spent, (C)  $\text{P}/\text{Ga-SiO}_2$  calcined, (D)  $\text{P}/\text{Ga-SiO}_2$  reduced, (E)  $\text{Ga-SiO}_2$  calcined, and (F)  $\text{Ga-SiO}_2$  reduced.

structure.

### 3.2. Activity test for HDS of 4,6-DMDBT

It is reported that the HDS of 4,6-DMDBT generates three main

products [22]. The 3,3'-dimethylbiphenyl (3,3-DMBP), is the product of direct desulfurization of 4,6-DMDBT, whereas other major products, 3,3'-dimethylbicyclohexyl (DMBCH) and 3-(3'-methylcyclohexyl)toluene (MCHT), are produced via hydrogenation followed by hydrodesulfurization pathways [21,22]. Prins et al. demonstrated that the DDS product of the HDS of 4,6-DMDBT, i.e. DMBP, increases with the progress of the reaction, but the product selectivity of DMBP to the remaining products of the HDS is rarely affected. It was found that DMBP, the HDS product of 4,6-DMDBT, was not further hydrogenated to DMCHB or DMBCH under the similar reaction conditions as our work [44,45]. The effect of S, N, and aromatics model compounds on the HDS reaction over the  $\text{Ni}_2\text{P}$  catalysts was well studied in our recent papers [17,43], in which the catalytic activities for the HDS of 4,6-DMDBT and tetralin were tested on the  $\text{Ni}_2\text{P}/\text{SiO}_2$  and  $\text{NiMoS}/\text{Al}_2\text{O}_3$  catalysts at 573 K and 3.1 MPa. The results showed that without N compounds in the feed, the  $\text{Ni}_2\text{P}/\text{SiO}_2$  catalyst exhibited much higher activities than the  $\text{NiMoS}/\text{Al}_2\text{O}_3$  catalyst in the HDS, with respective conversions of 97 and 60%. The addition of a quinoline led to a small decrease in the HDS conversion to 85% for the  $\text{Ni}_2\text{P}/\text{SiO}_2$  catalyst, but a large drop to 41% for the  $\text{NiMoS}/\text{Al}_2\text{O}_3$  catalyst. For  $\text{Ni}_2\text{P}/\text{SiO}_2$ , the HYD pathway in the desulfurization 4,6-DMDBT was dominant and was less inhibited by nitrogen than  $\text{NiMoS}/\text{Al}_2\text{O}_3$ , due to the moderate acidity of  $\text{Ni}_2\text{P}$  in the form of PO-H sites that are able to protonate N compounds [43].

Fig. 6 shows the HDS conversions and product selectivities with respect to HYD and DDS pathways over the  $\text{Ni}_2\text{P}/\text{SiO}_2$  and  $\text{Ni}_2\text{P}/\text{Ga-SiO}_2$  catalysts, in which the reaction temperature was varied. The  $\text{Ni}_2\text{P}/\text{SiO}_2$  catalyst exhibits a high HDS conversion over 99%. These results are consistent with previous studies that the  $\text{Ni}_2\text{P}/\text{SiO}_2$  catalysts show very high and stable HDS activities in 4,6-DMDBT under similar conditions [17,43]. The  $\text{Ni}_2\text{P}/\text{Ga-SiO}_2$  catalyst also shows a high HDS activity with no significant difference in the HDS conversion from that of the  $\text{Ni}_2\text{P}/\text{SiO}_2$  catalyst under the same condition. This indicates that the addition of a small amount (1.0 wt%) of Ga does not significantly affect the HDS activity of the  $\text{Ni}_2\text{P}$  catalyst. However, there is a clear difference in the product selectivities for the  $\text{Ni}_2\text{P}/\text{Ga-SiO}_2$ . The  $\text{Ni}_2\text{P}/\text{SiO}_2$  maintains a high HYD selectivity ranging from 87.1% to 73.5% with varying reaction temperatures from 613 to 643 K, indicating superior hydrogenation activity of  $\text{Ni}_2\text{P}$  catalyst. Although the  $\text{Ni}_2\text{P}/\text{Ga-SiO}_2$  catalyst shows a high HDS conversion over 99%, the product selectivity was found different from the  $\text{Ni}_2\text{P}/\text{SiO}_2$  catalyst. At 613 K, the DDS selectivity of  $\text{Ni}_2\text{P}/\text{Ga-SiO}_2$  was higher than  $\text{Ni}_2\text{P}/\text{SiO}_2$  catalyst (16.4% vs. 12.9%). Moreover, upon the increase of the reaction temperature from 613 to 643 K, the product selectivity toward DDS pathway was further increased from 16.4% to 32.1%, while maintaining the high HDS conversion over 99%. The activation energies of the catalysts for the DDS pathway in the HDS of 4,6-DMDBT were obtained as shown in Fig. 6 and Table 2. It is noted that the  $\text{Ni}_2\text{P}/\text{Ga-SiO}_2$  catalyst shows a lower activation energy than the  $\text{Ni}_2\text{P}/\text{SiO}_2$  catalyst (86.3 vs. 88.0 kJ/mol) for the DDS of 4,6-DMDBT. These results imply that the addition of Ga to the  $\text{Ni}_2\text{P}$  catalyst affects the HDS pathways of 4,6-DMDBT, thereby promoting DDS and allowing less  $\text{H}_2$  consumption. The Ga effect was prominent at a loading level up to 1.0 wt%, while a higher Ga loading did not significantly affect the HDS selectivity as shown in Fig. S2 of supplementary materials.

According to previous studies, the activation of the DDS pathway of thiophenic sulfur e.g. DBT or 4,6-DMDBT is originated from the S atom adsorbing onto the catalytic active sites, then forming  $\sigma$ -bond, which leads to C-S bond cleavage [3,18]. The  $\sigma$ -bond formation of the thiophenic sulfur with the active site is facilitated particularly on the electron deficient site where the lone electron pair of the S atom can easily adsorb [3,18]. This implies that the electron deficiency of the catalyst center is advantageous for the DDS selectivity. On the other hand, if the electron density of the active center is sufficient, it forms the  $\pi$ -bond with the benzene ring of the benzothiophenic molecules, so the C=C bond of aromatics is saturated first followed by C-S bond cleavage, i.e. following the HYD pathway. In this context, the high DDS

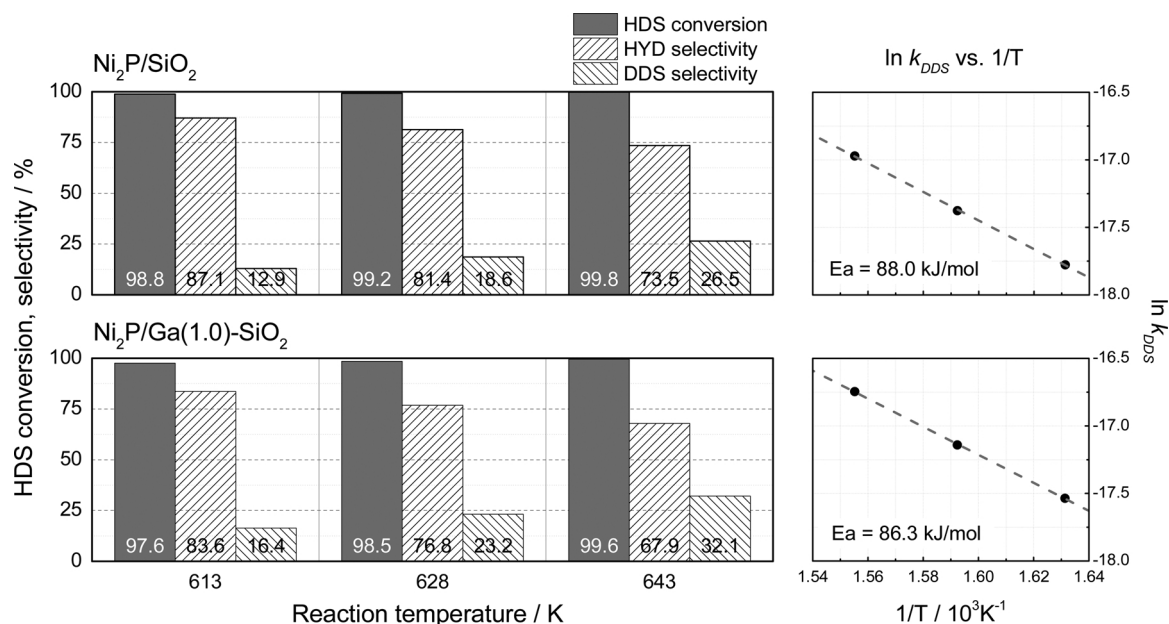


**Fig. 6.** HDS performance of Ni<sub>2</sub>P/SiO<sub>2</sub> and Ni<sub>2</sub>P/Ga-SiO<sub>2</sub> at 3.0 MPa and at different temperature of 613, 628, and 643 K; H<sub>2</sub> / feed ratio (gas flow rate / liquid flow ratio) = 1500 at 50 cm<sup>3</sup>min<sup>-1</sup> H<sub>2</sub>.

**Table 2**

Activation energies of the catalyst samples for the DDS pathway in the HDS of 4,6-DMDS.

Catalyst	T (K)	DDS Yield (%)	$K_{DDS}^a$ (m <sup>3</sup> /kg-sec)	$E_a^b$ (kJ·mol <sup>-1</sup> )	R <sup>2</sup>
Ni <sub>2</sub> P/SiO <sub>2</sub>	613	12.8	1.9023E-08	88.0	0.999
	628	18.5	2.8412E-08		
	643	26.4	4.2573E-08		
Ni <sub>2</sub> P/Ga-SiO <sub>2</sub>	613	16.0	2.4216E-08	86.3	0.999
	628	22.8	3.5940E-08		
	643	31.9	5.3360E-08		

selectivity of Ni<sub>2</sub>P/Ga-SiO<sub>2</sub> might be influenced by the change of the electron density of the catalyst caused by the addition of Ga species, which promotes the adsorption of S to the active site.

### 3.3. Electron deficient nature of Ni<sub>2</sub>P/Ga-SiO<sub>2</sub>

FTIR studies of CO adsorption on the catalysts are useful for the characterization of the electronic properties of transition metal species [27]. It is reported that the IR bands for Ni<sup>n+</sup>-CO complexes are observed in the wavenumber region of 2220–2000 cm<sup>-1</sup>, where four main vibrational bands for linearly adsorbed CO species on Ni atoms are found depending on the oxidation state of the Ni [14,27,43]. The adsorption of CO on the Ni atoms with a higher oxidation state, as carbonyl complexes of Ni<sup>3+</sup>-CO and Ni<sup>0</sup>-CO, is observed to give IR bands at around 2155 and 2136 cm<sup>-1</sup>, respectively, but they are visible only at low temperatures due to a weak interaction [27]. For the Ni atoms with a low oxidation state, the carbonyl complexes assigned to Ni<sup>+</sup>-CO and Ni<sup>0</sup>-CO give rise to IR bands at around 2130 and 2065 cm<sup>-1</sup>, respectively, which are relatively stable [27]. The IR band shift to higher frequency indicate that CO is bonded mainly by an electrostatic interaction or a  $\sigma$ -bond to the Ni species with a higher oxidation state, while the shift to lower frequency suggests the presence of  $\pi$  back-bonding

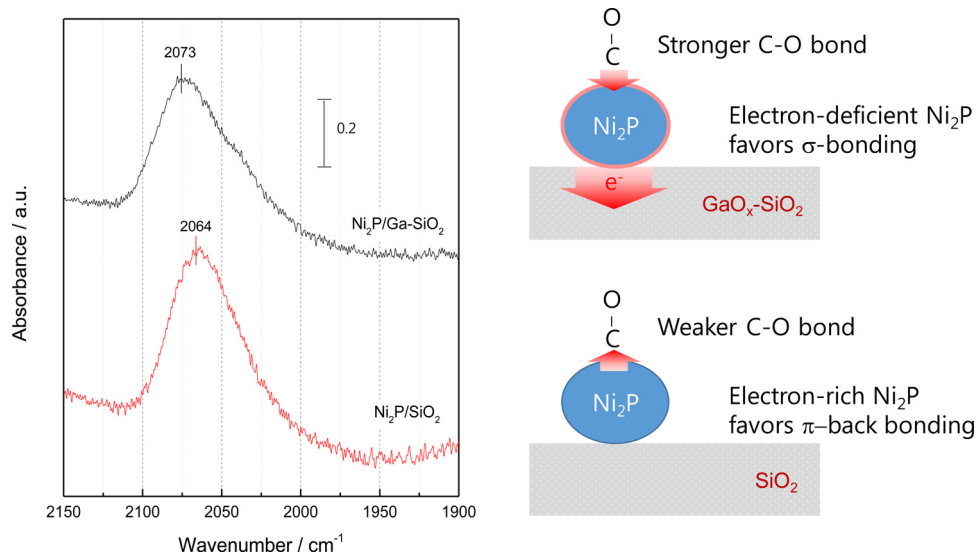


**Fig. 7.** In situ FTIR spectra with CO chemisorption of Ni<sub>2</sub>P/SiO<sub>2</sub> and Ni<sub>2</sub>P/Ga-SiO<sub>2</sub>.



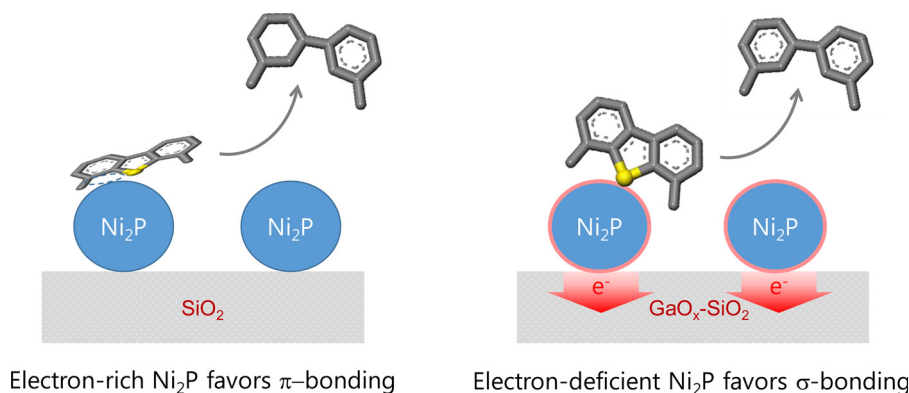


Fig. 8. Proposed reaction mechanism of HDS over Ni<sub>2</sub>P/SiO<sub>2</sub> and Ni<sub>2</sub>P/Ga-SiO<sub>2</sub>.

due to the higher *d*-electron density of the Ni species with a lower oxidation state.

Fig. 7 shows the CO adsorbed FTIR spectra of Ni<sub>2</sub>P/SiO<sub>2</sub> and Ni<sub>2</sub>P/Ga-SiO<sub>2</sub>. The Ni<sub>2</sub>P/SiO<sub>2</sub> catalyst shows a stronger IR band at 2064 cm<sup>-1</sup>, which is assigned to a linearly adsorbed CO on Ni species of Ni<sub>2</sub>P. A previous study of CO chemisorption on Ni<sub>2</sub>P/SiO<sub>2</sub> has revealed that the IR band of CO vibration shifts to lower frequencies than NiS/SiO<sub>2</sub>, due to the electron-rich nature of Ni<sub>2</sub>P causing  $\pi$  back-bonding between CO and Ni species [27]. The Ni<sub>2</sub>P/Ga-SiO<sub>2</sub> catalyst shows a relatively weaker IR band at 2073 cm<sup>-1</sup>, which appears at slightly higher frequency than that of the Ni<sub>2</sub>P/SiO<sub>2</sub> catalyst. The Ni<sub>2</sub>P samples with different Ga loadings of 0.5 and 2.0 wt% also exhibited similar results of peak shifts to higher frequencies but are furthest with the 1.0 wt% Ga sample (Fig. S3). The IR band shift to a higher frequency indicates a low electron density on the adsorbing metal sites. These results demonstrate the Ni<sub>2</sub>P catalyst supported on Ga-SiO<sub>2</sub> shows an electron-deficient nature induced by electron-withdrawing GaOx species (Fig. 8).

Overall, these results suggest that the high DDS selectivity of Ni<sub>2</sub>P/Ga-SiO<sub>2</sub> is attributed to the lack of electrons in the Ni<sub>2</sub>P phase due to GaOx, leading to the formation of  $\sigma$ -bonding of S with the active site. Furthermore, it also indicates that the surface electron density of Ni<sub>2</sub>P catalyst can be controlled by the addition of Ga.

#### 4. Conclusions

Nickel phosphide (Ni<sub>2</sub>P) catalysts supported on SiO<sub>2</sub> and Ga-SiO<sub>2</sub> showed a high HDS activity for 4,6-DMDBT at 613–643 K and 3.0 MPa. The dispersion of the Ni<sub>2</sub>P catalysts was found almost identical regardless of Ga addition. The desulfurization occurred preferentially by the hydrogenation (HYD) pathway for the Ni<sub>2</sub>P catalyst. In contrast, the direct desulfurization (DDS) pathway was promoted over the Ni<sub>2</sub>P/Ga-SiO<sub>2</sub> catalyst followed, which is ascribed to the electron-deficiency of Ni<sub>2</sub>P caused by GaOx. These results thus suggest that in the Ni<sub>2</sub>P phase the electron-deficient Ni sites are responsible for desulfurization by the DDS pathway by taking a sulfur atom of 4,6-DMDBT, while the electron-rich Ni sites favor  $\pi$ -bonding with aromatic ring of 4,6-DMDBT facilitating the HDS by the HYD pathway.

#### Acknowledgements

The authors acknowledge the financial supports from the Korea Institute of Energy Technology Evaluation and Planning (KETEP-20154030200830) and the National Research Foundation of Korea (NRF-2019R1A2C2009999), Ministry of Trade, Industry & Energy of Korea (MOTIE-10082582).

#### Appendix A. Supplementary data

Supplementary material related to this article can be found, in the online version, at doi:<https://doi.org/10.1016/j.apcatb.2019.01.087>.

#### References

- [1] C. Song, An overview of new approaches to deep desulfurization for ultra-clean gasoline, diesel fuel and jet fuel, *Catal. Today* 86 (2003) 211–263.
- [2] A. Infantes-Molina, J.A. Cecilia, B. Pawelec, J.L.G. Fierro, E. Rodríguez-Castellón, A. Jiménez-López, Ni<sub>2</sub>P and CoP catalysts prepared from phosphite-type precursors for HDS-HDN competitive reactions, *Appl. Catal. A Gen.* 390 (2010) 253–263.
- [3] A. Stanislaus, A. Marafi, M.S. Rana, Recent advances in the science and technology of ultra low sulfur diesel (ULSD) production, *Catal. Today* 153 (2010) 1–68.
- [4] R. Javadli, A. de Klerk, Desulfurization of heavy oil, *Appl. Petrochemical Res.* 1 (2012) 3–19.
- [5] E. US, Control of Air Pollution From Motor Vehicles: Tier 3 Motor Vehicle Emission and Fuel Standards; Final Rule, *Epa Usa*, (2014) <https://www.epa.gov/regulations-emissions-vehicles-and-engines/final-rule-control-air-pollution-motor-vehicles-tier-3>.
- [6] Council of the European Union, Directive 2009/28/EC of the European Parliament and of the Council of 23 April 2009, *Off. J. Eur. Union* (2009), <https://eur-lex.europa.eu/legal-content/en/ALL/?uri=CELEX:31993L0012>.
- [7] S.A. Ganiyu, K. Alhooshani, S. Ahmed, Single-pot synthesis of Ti-SBA-15-NiMo hydrodesulfurization catalysts: role of calcination temperature on dispersion and activity, *Appl. Catal. B Environ.* 203 (2017) 428–441.
- [8] W. Zhou, Q. Wei, Y. Zhou, M. Liu, S. Ding, Q. Yang, Hydrodesulfurization of 4, 6-dimethyldibenzothiophene over NiMo sulfide catalysts supported on meso-microporous Y zeolite with different mesopore sizes, *Appl. Catal. B Environ.* 238 (2018) 212–224.
- [9] T. Huang, J. Xu, Y. Fan, Effects of concentration and microstructure of active phases on the selective hydrodesulfurization performance of sulfided CoMo/Al<sub>2</sub>O<sub>3</sub> catalysts, *Appl. Catal. B Environ.* 220 (2018) 42–56.
- [10] H.E. Lindstad, C.F. Rehn, G.S. Eskeland, Sulphur abatement globally in maritime shipping, *Transp. Res. Part D Transp. Environ.* 57 (2017) 303–313.
- [11] P. Grange, Catalytic hydrodesulfurization, *Catal. Rev.* 21 (1980) 135–181.
- [12] D. Liu, A. Wang, C. Liu, R. Prins, Ni<sub>2</sub>P/Al<sub>2</sub>O<sub>3</sub> hydrodesulfurization catalysts prepared by separating the nickel compound and hypophosphite, *Catal. Today* 292 (2017) 133–142.
- [13] S.T. Oyama, T. Gott, H. Zhao, Y.-K. Lee, Transition metal phosphide hydroprocessing catalysts: a review, *Catal. Today* 143 (2009) 94–107.
- [14] S.J. Sawhill, K.A. Layman, D.R. Van Wyk, M.H. Engelhard, C. Wang, M.E. Bussell, Thiophene hydrodesulfurization over nickel phosphide catalysts: effect of the precursor composition and support, *J. Catal.* 231 (2005) 300–313.
- [15] S.T. Oyama, Y.-K. Lee, The active site of nickel phosphide catalysts for the hydrodesulfurization of 4,6-DMDBT, *J. Catal.* 258 (2008) 393–400.
- [16] S. Yang, C. Liang, R. Prins, A novel approach to synthesizing highly active Ni<sub>2</sub>P/SiO<sub>2</sub> hydrotreating catalysts, *J. Catal.* 237 (2006) 118–130.
- [17] Y.-K. Lee, S.T. Oyama, Sulfur resistant nature of Ni<sub>2</sub>P catalyst in deep hydrodesulfurization, *Appl. Catal. A Gen.* 548 (2017) 103–113.
- [18] A. Mansouri, N. Semagina, Enhancement of palladium-catalyzed direct desulfurization by yttrium addition, *Appl. Catal. A Gen.* 543 (2017) 43–50.
- [19] D. Whitehurst, T. Isoda, I. Mochida, Present state of the art and future challenges in the hydrodesulfurization of polyaromatic sulfur compounds, *J. Adv. Catal. Sci. Technol.* 42 (1998) 345–471.
- [20] B.C. Gates, H. Topsøe, Reactivities in deep catalytic hydrodesulfurization: challenges, opportunities, and the importance of 4-methyldibenzothiophene and 4,6-dimethyldibenzothiophene, *Polyhedron* 16 (1997) 3213–3217.
- [21] M. Egorova, R. Prins, Competitive hydrodesulfurization of 4,6-dimethyldibenzothiophene, hydrodenitrogenation of 2-methylpyridine, and hydrogenation of naphthalene over sulfided NiMo/γ-Al<sub>2</sub>O<sub>3</sub>, *J. Catal.* 224 (2004) 278–287.
- [22] J.H. Kim, X. Ma, C. Song, Y.-K. Lee, S.T. Oyama, Kinetics of two pathways for 4,6-

- dimethyldibenzothiophene hydrodesulfurization over NiMo, CoMo sulfide, and nickel phosphide catalysts, *Energy Fuels* 19 (2005) 353–364.
- [23] Y.-K. Lee, Y. Shu, S.T. Oyama, Active phase of a nickel phosphide (Ni<sub>2</sub>P) catalyst supported on KUSY zeolite for the hydrodesulfurization of 4,6-DMDBT, *Appl. Catal. A Gen.* 322 (2007) 191–204.
- [24] I.I. Abu, K.J. Smith, The effect of cobalt addition to bulk MoP and Ni<sub>2</sub>P catalysts for the hydrodesulfurization of 4,6-dimethyldibenzothiophene, *J. Catal.* 241 (2006) 356–366.
- [25] S. Ted Oyama, H. Zhao, H.J. Freund, K. Asakura, R. Włodarczyk, M. Sierka, Unprecedented selectivity to the direct desulfurization (DDS) pathway in a highly active FeNi bimetallic phosphide catalyst, *J. Catal.* 285 (2012) 1–5.
- [26] Q. Li, P. Wu, L. Lan, N. Wei, S. Ji, Preparation of novel mesoporous Ce-Ni<sub>2</sub>P/SBA-15 catalysts and their catalytic performance for hydrodesulfurization of dibenzothiophene, *Appl. Petrochem. Res.* 4 (2014) 209–216.
- [27] H. Zhao, S.T. Oyama, H.J. Freund, R. Włodarczyk, M. Sierka, Nature of active sites in Ni<sub>2</sub>P hydrotreating catalysts as probed by iron substitution, *Appl. Catal. B Environ.* 164 (2015) 204–216.
- [28] E. Altamirano, J.A. de los Reyes, F. Murrieta, M. Vrinat, Hydrodesulfurization of 4,6-dimethyldibenzothiophene over Co(Ni)MoS<sub>2</sub> catalysts supported on alumina: effect of gallium as an additive, *Catal. Today* 133–135 (2008) 292–298.
- [29] W. Zhou, M. Liu, Q. Zhang, Q. Wei, S. Ding, Y. Zhou, Synthesis of NiMo catalysts supported on gallium-containing mesoporous  $\gamma$  zeolites with different gallium contents and their high activities in the hydrodesulfurization of 4,6-Dimethyldibenzothiophene, *ACS Catal.* 7 (2017) 7665–7679.
- [30] E. Altamirano, J.A. De Los Reyes, F. Murrieta, M. Vrinat, Hydrodesulfurization of dibenzothiophene and 4,6-dimethyl-dibenzothiophene: gallium effect over NiMo/Al<sub>2</sub>O<sub>3</sub> sulfided catalysts, *J. Catal.* 235 (2005) 403–412.
- [31] J.N. Díaz de León, M. Picquart, M. Villarroel, M. Vrinat, F.J. Gil Llambias, F. Murrieta, J.A. de los Reyes, Effect of gallium as an additive in hydrodesulfurization WS<sub>2</sub>/γ-Al<sub>2</sub>O<sub>3</sub> catalysts, *J. Mol. Catal. A Chem.* 323 (2010) 1–6.
- [32] J.N. Díaz De León, M. Picquart, L. Massin, M. Vrinat, J.A. De Los Reyes, Hydrodesulfurization of sulfur refractory compounds: effect of gallium as an additive in NiWS/γ-Al<sub>2</sub>O<sub>3</sub> catalysts, *J. Mol. Catal. A Chem.* 363–364 (2012) 311–321.
- [33] Y.-S. Kim, K.-S. Cho, Y.-K. Lee, Morphology effect of  $\beta$ -zeolite supports for Ni<sub>2</sub>P catalysts on the hydrocracking of polycyclic aromatic hydrocarbons to benzene, toluene, and xylene, *J. Catal.* 351 (2017) 67–78.
- [34] Y. Yang, J. Chen, H. Shi, Deoxygenation of methyl laurate as a model compound to hydrocarbons on Ni<sub>2</sub>P/SiO<sub>2</sub>, Ni<sub>2</sub>P/MCM-41, and Ni<sub>2</sub>P/SBA-15 catalysts with different dispersions, *Energy Fuels* 27 (2013) 3400–3409.
- [35] S.T. Oyama, X. Wang, Y.-K. Lee, K. Bando, F.G. Requejo, Effect of phosphorus content in nickel phosphide catalysts studied by XAFS and other techniques, *J. Catal.* 210 (2002) 207–217.
- [36] C.T. Shao, W.Z. Lang, X. Yan, Y.J. Guo, Catalytic performance of gallium oxide based-catalysts for the propane dehydrogenation reaction: effects of support and loading amount, *RSC Adv.* 7 (2017) 4710–4723.
- [37] S.T. Oyama, X. Wang, Y.-K. Lee, W.J. Chun, Active phase of Ni<sub>2</sub>P/SiO<sub>2</sub> in hydroprocessing reactions, *J. Catal.* 221 (2004) 263–273.
- [38] K.-S. Cho, Y.-K. Lee, XAFS studies on highly dispersed Ni<sub>2</sub>P/SiO<sub>2</sub> catalysts for hydrodesulfurization of 4,6-dimethyldibenzothiophene, *Nucl. Instrum. Methods Phys. Res. Sect. A Accel. Spectrometers Detect. Assoc. Equip.* 621 (2010) 690–694.
- [39] N.M.D. Brown, G.N. Mcmonagle, G.N. Greaves, An absorption edge and extended X-ray absorption fine structure study of a dispersed manganese dioxide oxidation catalyst, *J. Chem. Soc. Faraday Trans 1* (80) (1984) 589–597.
- [40] A. Getsoian, U. Das, J. Camacho-Bunquin, G. Zhang, J.R. Gallagher, B. Hu, S. Cheah, J.A. Schaidle, D.A. Ruddy, J.E. Hensley, T.R. Krause, L.A. Curtiss, J.T. Miller, A.S. Hock, Organometallic model complexes elucidate the active gallium species in alkane dehydrogenation catalysts based on ligand effects in Ga K-edge XANES, *Catal. Sci. Technol.* 6 (2016) 6339–6353.
- [41] F. Tourtin, A. Ibanez, A. Haidoux, E. Philippot, Local range order in thin dielectric films of gallium phosphate, *Thin Solid Films* 279 (1996) 59–65.
- [42] P. Charton, P. Armand, X-ray absorption and Raman characterizations of TeO<sub>2</sub>-Ga<sub>2</sub>O<sub>3</sub> glasses, *J. Non. Solids* 356 (2010) 307–315.
- [43] Y.-K. Lee, S.T. Oyama, Bifunctional nature of a SiO<sub>2</sub>-supported Ni<sub>2</sub>P catalyst for hydrotreating: EXAFS and FTIR studies, *J. Catal.* 239 (2006) 376–389.
- [44] L. Yang, X. Li, A. Wang, R. Prins, Y. Wang, Y. Chen, X. Duan, Its hydrogenated intermediates over bulk Ni<sub>2</sub>P, *J. Catal.* 317 (2014) 144–152.
- [45] X. Li, A. Wang, M. Egorova, R. Prins, Kinetics of the HDS of 4,6-dimethyldibenzothiophene and its hydrogenated intermediates over sulfided Mo and NiMo on γ-Al<sub>2</sub>O<sub>3</sub>, *J. Catal.* 250 (2007) 283–293.